Correction method of measurement volume effects on time-averaged statistics for laser Doppler velocimetry

Yuki Wada,[1,*] Noriyuki Furuichi,[2] and Yoshiyuki Tsuji[3]

[1] *Japan Atomic Energy Agency, 2-4 Shirakata, Tokai-mura, Naka-gun, Ibaraki 319-1195, Japan*

[2] *Advanced Industrial Science and Technology, National Metrology Institute of Japan, 1-1-1 Umezono, Tsukuba-shi, Ibaraki 305-8563, Japan*

[3] *Department of Engineering Nagoya University, Furo-cho, Chikusa-ku, Nagoya-shi, Aichi 464-8603, Japan*

A new correction method for laser Doppler velocimetry (LDV) measurement volume effects on the time-averaged velocity statistics is proposed by considering the probability density function of streamwise fluctuating velocity and the streamwise cross-sectional area of the measurement volume. The proposed correction method is fundamentally different from previous correction methods using a laser intensity profile of LDV. We propose a simple equation to correct the measurement volume effects. By using the equation and calculating both measurement locations and volumes precisely, the correction for the measurement volume effects on time-averaged velocity statistics can be performed on the basis of LDV measurement data. By comparing with the correction method proposed by Durst *et al*. [J. Fluid Mech. **295**, 305 (1995)], the two correction methods provide almost the same results. In addition, the validity and applicability to high Reynolds numbers or low spatial resolution conditions of the two correction methods are confirmed.

Keywords: LDV, Correction method, Turbulence intensity, PDF, Pipe flow

1. Introduction

Recently, high Reynolds number turbulent pipe flow experiments have been studied in several facilities (Superpipe [1], CICLoPE [2], and Hi-Reff [3]). The velocity measurements of turbulent pipe flow field have been conducted by Pitot tube [1,4], hot wire anemometry (HWA) [5–7], laser Doppler velocimetry (LDV) [8,9], and particle image velocimetry (PIV) [10]. In high Reynolds number experiments, the spatial resolution of a measurement device is crucial. Generally, the higher the Reynolds number in the experiment performed, the smaller the measurement volume required. As shown in previous studies, the spatial resolution of a measurement device influences the statistics, especially for the turbulence intensity (TI) [8,11,12]. Since minimizing a measurement volume has a physical limitation, the correction method for each measurement device should be studied to obtain reliable experimental data for high Reynolds numbers.

* wada.yuki@jaea.go.jp

HWA is one of the most common flow velocity measurement techniques and has long been applied to high Reynolds number experiments. Therefore, the spatial resolution issue for HWA has been discussed by several researchers in terms of high Reynolds number experiments [13–15]. In principle, the velocity measured by HWA would be averaged within the sensing length. Therefore, the correction method for time series of velocity fluctuations based on the spectral consideration, etc. has been proposed [16,17]. In contrast, since LDV has rarely been applied to high Reynolds number experiments, the spatial resolution issue for LDV in terms of high Reynolds number experiments was less active than that for HWA. Moreover, since the measurement principle of LDV fundamentally differs from that of HWA, the same correction method with HWA could not be applied to LDV measurement data. To the best of our knowledge, only one correction method for LDV measurement volume effects has been proposed by Durst *et al.* [8]. The Durst correction method for TI profile uses the wall-normal length of measurement volume and the wall-normal derivatives of mean velocity and TI profiles. In application, Fischer *et al.* [9] used the Durst method to correct velocity statistics and discuss higher-order moments of measurement velocities using the experimental data at low Reynolds numbers ($Re_\tau < 500$).

We have reported the friction factor and a few characteristics of the mean velocity profile up to $Re_\tau = 20000$ in previous studies [3,18]. We are also interested in TI profiles, such as the Reynolds number dependence of inner peaks and outer logarithmic relations. However, it is impossible to accurately discuss such characteristics of the TI profiles at high Reynolds numbers because the TI profiles are significantly affected by spatial resolution. Therefore, the spatial resolution issues of LDV measurement should be clarified. There are two considerable aspects regarding correction methods. One is the Reynolds number effect. Although the Durst method has been applied to the several experimental data measured by LDV, they are performed under low Reynolds numbers; the validity for and applicability to the experimental data at high Reynolds numbers has not been confirmed. The other is the effect of inclined measurement volume against the wall. Since the LDV measurement angle in the present experiment conducted at Hi-Reff was inclined from the wall, the applicability of the correction method should be discussed. However, there is no method to guarantee the corrected value, even if the Durst method applies to the various ranges of Reynolds number experimental data. To validate and confirm the applicability of correction methods, alternative correction concepts and methods are strongly required.

In this study, we propose a new correction method based on PDF and two-dimensional geometric considerations for the LDV measurement volume effects and apply it to data under high Reynolds numbers or low spatial resolution compared with the Durst method. The data were measured by LDV in high Reynolds number turbulent pipe flow up to $Re_\tau = 10000$. Further, we discuss the applicability to the inclination measurement volume setup.

2. Experimental conditions and data processing method

2.1. Experimental facility and equipment

Experiments were conducted using "Hi-Reff" [19] at Advanced Industrial Science and Technology. The pipe used was made of stainless steel and had a 100 mm inner diameter; the inner surface was polished, and it had a 0.8 μm average roughness. The inlet length was about 11 m, thus the ratio of the inlet length to the inner diameter was approximately 110, which was adequate to remove the effect of the inlet condition on the flow field at the test section. The maximum flow rate using the pipe was 300 m^3/h, and the bulk Reynolds number was approximately 10^6 in the pipe. For more details of the experimental setup, refer to our previous study [3].

In this experiment, the working fluid was water. The LDV system (BSA Flow Software Version 4.10) produced by DANTEC was used for velocity measurement. The measurable velocity component was the streamwise direction. The wavelength of the laser λ_L was 514.5 nm; the laser beam diameter at an inducing collecting lens D_L was 2.2 mm; the spacing of the laser beams at the collecting lens was 38.998 mm; the focal length of the collecting lens f was 160 mm. The measurement volume of the LDV system was an ellipsoidal body, the short axis length of the body was calculated as $4\lambda_L f / \pi D_L$. In the experimental setup, the short and long axis lengths of the body were calculated as 47.6 and 524.9 μm, respectively. A three-dimensional moving system, whose resolution was 1/160 mm/pulse, was used.

2.2. Experimental condition

The measurement path was set to 46 locations, where 46 locations were determined as almost equal spacing in logarithmic scale from the pipe wall to the center of the test section. To measure velocity profiles in the test section by different measurement volumes, especially in the wall-normal direction, velocity profile measurements were conducted in different measurement paths of the LDV moving system (Fig. 1) to discuss the LDV measurement volume effects. Table 1 shows the relation between the angle of measurement paths θ_{path} and spatial resolution d^+ at $Re_\tau = 3200$. In this study, d is the wall-normal length of the theoretical measurement volume. Three different measurement paths of 15°, 18°, and 20° against the vertical axis were employed to discuss the LDV measurement volume effect. They were called Cases 1–3 for convenience.

The experimental flow conditions were the following four Reynolds numbers: $Re_\tau = 3200$, 3900, 5800, and 10400 ($1.4 \times 10^5 \leqq Re_b \leqq 5.2 \times 10^5$, $Re_\tau = u_\tau R / \nu$, $Re_b = U_b 2R / \nu$, where U_b : cross-sectional averaged velocity, u_τ : friction velocity, R : radius of the pipe, ν : kinematic viscosity).

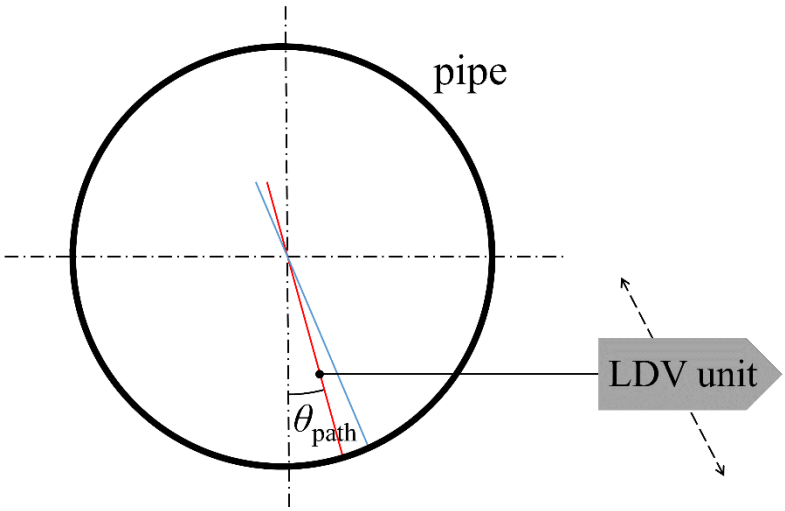

Fig. 1. Schematic view of the measurement path for different volume sizes in the wall-normal direction. The red and blue lines indicate different measurement paths, which correspond to using different measurement volumes in the wall-normal direction, respectively.

TABLE 1. Spatial resolution conditions.

Case number	Spatial resolution level	θ_{path}	d^+ at $y^+ = 15$, $Re_\tau = 3200$
Case 1	High	≈15°	≈5.3
Case 2	Mid	≈18°	≈7.9
Case 3	Low	≈20°	≈9.8

3. Correction concept and procedure

A correction method for the LDV measurement volume effect was reported by Durst *et al.* [8]; to the best of our knowledge, it is the only correction method. The validity of the Durst method has been confirmed by several experimental data at low Reynolds numbers, but its applicability has not been confirmed at high Reynolds numbers. Therefore, we proposed an alternative correction method based on the concept of PDF profiles of velocity fluctuations and the geometric considerations of measurement volumes. Our correction method is compared with that of Durst in high Reynolds number flow, and we realize that the TI is overestimated close to the wall due to the measurement volume effect. This overestimation improves when the measurement volume effect was corrected adequately.

3.1. Effect of LDV measurement volume

First, we considered the time series of the streamwise velocities measured via the LDV in the infinitely minimal measurement volume. If the tracer particles were sufficiently small and the measuring time was sufficiently long, the PDFs calculated using the time series of the streamwise velocities were close to the true PDFs of the streamwise velocities at an arbitrary measuring location, as expressed by Eq. (1).

$$P_{\mathrm{T}}(u;\boldsymbol{x}) = \lim_{T\to\infty}\frac{1}{T}\int_{t=0}^{T} p_1(u;\boldsymbol{x},t)dt, \tag{1}$$

where u is the sample variable in the velocity space, $\boldsymbol{x} = (x, y, z)$, and p_1 is defined by the delta function as Eq. (2). It is called a fine-grained PDF of velocity [20].

$$p_1(u;\boldsymbol{x},t) \equiv \delta(U(\boldsymbol{x},t) - u), \tag{2}$$

where U is an instantaneous random velocity fluctuation. Hereinafter, we define $P_{\mathrm{T}}(u;\boldsymbol{x})$ as the "true" PDF at point $\boldsymbol{x}$.

Next, we considered a situation of measuring streamwise velocity inside a finite volume of $\boldsymbol{V}$. The shape of the finite volume was an ellipsoid; Fig. 2 (a) shows a schematic image of the three-dimensional LDV measurement volume when the tracer particle passed through it. The streamwise direction was *x*, and the particle (black solid circle) moved along the x-axis. The LDV could only measure the velocity of the tracer particle at the cross-section of the ellipsoid, which was a two-dimensional set of $\boldsymbol{V}$ and was expressed as $\boldsymbol{S}$. When the flow was fully developed, the velocity PDF was independent of streamwise position. Therefore, it was sufficient to analyze the velocity inside $\boldsymbol{S}$ [Fig. 2 (b)]. A PDF of the streamwise velocity in volume $\boldsymbol{V}$ was expressed by the summation of the true PDF at $\boldsymbol{x}$ inside $\boldsymbol{S}$ with multiplying a probability$P_2(\boldsymbol{x} \in \boldsymbol{S})$. $P_2(\boldsymbol{x} \in \boldsymbol{S})$ is the probability when a tracer particle locates inside $\boldsymbol{S}$. Then, the PDF measured by the LDV with a finite volume can be expressed by Eq. (3). Notably, $P_{\mathrm{M}}(u, \boldsymbol{S})$ was different from the true PDF and was a weighted average of $P_{\mathrm{T}}(u;\boldsymbol{x})$.

$$P_{\mathrm{M}}(u;\boldsymbol{V}) = P_{\mathrm{M}}(u;\boldsymbol{S}) = \sum_{\boldsymbol{x}\in\boldsymbol{S}} P_{\mathrm{T}}(u;\boldsymbol{x})P_2(\boldsymbol{x}) \tag{3}$$

Since the tracer particles passed through $\boldsymbol{S}$ uniformly, the probability $P_2(\boldsymbol{x} \in \boldsymbol{S})$ should be equal to $\Delta S/S$, where ΔS was a small area centered at $\boldsymbol{x}$, as indicated by the red circle in Fig. 2 (b), and S was the area of $\boldsymbol{S}$, that is, $S = |\boldsymbol{S}|$. Accordingly, Eq. (3) is rewritten as follows:

$$P_{\mathrm{M}}(u;\boldsymbol{V}) = P_{\mathrm{M}}(u;\boldsymbol{S}) = \lim_{\Delta S\to 0}\sum_{\boldsymbol{x}\in\boldsymbol{S}} P_{\mathrm{T}}(u;\boldsymbol{x})\frac{\Delta S}{S} = \frac{1}{S}\int_{\boldsymbol{S}} P_{\mathrm{T}}(u;\boldsymbol{x})dS \tag{4}$$

The PDF measured by LDV with the finite volume size $\boldsymbol{V}$ could be written by an integral formula by Eq. (4). Therefore, this suggested that the measured PDF could be expressed as a cross-sectional surface average of the true PDFs.

In the steady flow fields where the instantaneous streamwise velocity is sufficiently larger than other two velocity components, Eq. (4) is satisfied. The "true" PDFs are obtained to solve Eq. (4) as an inverse problem. In this study, we demonstrate that the measured PDFs are reconstructed using the true PDFs using Eq. (4).

3.2. Simplification of Equation (4) for application to wall turbulence

In the pipe flow, the statistical quantities did not change because of the homogeneity along the circumferential direction. Thus, the dimension of the integral in Eq. (4) could be reduced to one dimension as follows:

$$P_{\mathrm{M}}(u;\boldsymbol{V}) = P_{\mathrm{M}}(u;\boldsymbol{S}) = \lim_{\Delta y\to 0}\sum_{y=y_{\mathrm{c}}-D/2}^{y_{\mathrm{c}}+D/2} P_{\mathrm{T}}(u;y)\frac{l(y,\boldsymbol{S})\Delta y}{S} = \frac{1}{S}\int_{y_{\mathrm{c}}-D/2}^{y_{\mathrm{c}}+D/2} P_{\mathrm{T}}(u;y)l(y,\boldsymbol{S})dy, \tag{5}$$

where y is the wall-normal location, y_{c} is the center of $\boldsymbol{S}$, D is the wall-normal length of $\boldsymbol{S}$, and l is the length of the spanwise or circumferential direction within $\boldsymbol{S}$ at the wall-normal location of y [Fig. 2 (c)].

Several parameters in Eq. (5) were normalized by inner variables; Eq. (5) could be rewritten as Eq. (6). The schematic image is shown in Fig. 2 (d). Equation (6) describes a formula to obtain a streamwise velocity PDF: P_{M} measured by the LDV with the finite size measurement volume.

$$P_{\mathrm{M}}(u^+;y_{\mathrm{c}}^+,d^+) = \frac{1}{S}\int_{y_{\mathrm{c}}^+-\frac{d^+}{2}}^{y_{\mathrm{c}}^++\frac{d^+}{2}}\{P_{\mathrm{T}}(u^+,y'^+)\times l(y_{\mathrm{c}}^+,y'^+)\}dy'^+ \tag{6}$$

Figure 2 (d) shows the schematic illustration of the coordinate of the present measurement volume. The red line indicates a boundary of the measurement volume of the LDV system in the streamwise cross-section; the area enclosed by the red line is S in Eq. (6); the black dot indicates a focal point of the LDV system that is equal to the measurement point of y_{c}^+; the dashed line indicates the spanwise length l of the measurement volume, which is a function of y_{c}^+ and y'^+, where y'^+ is a vertical location in the coordinate of y^+.

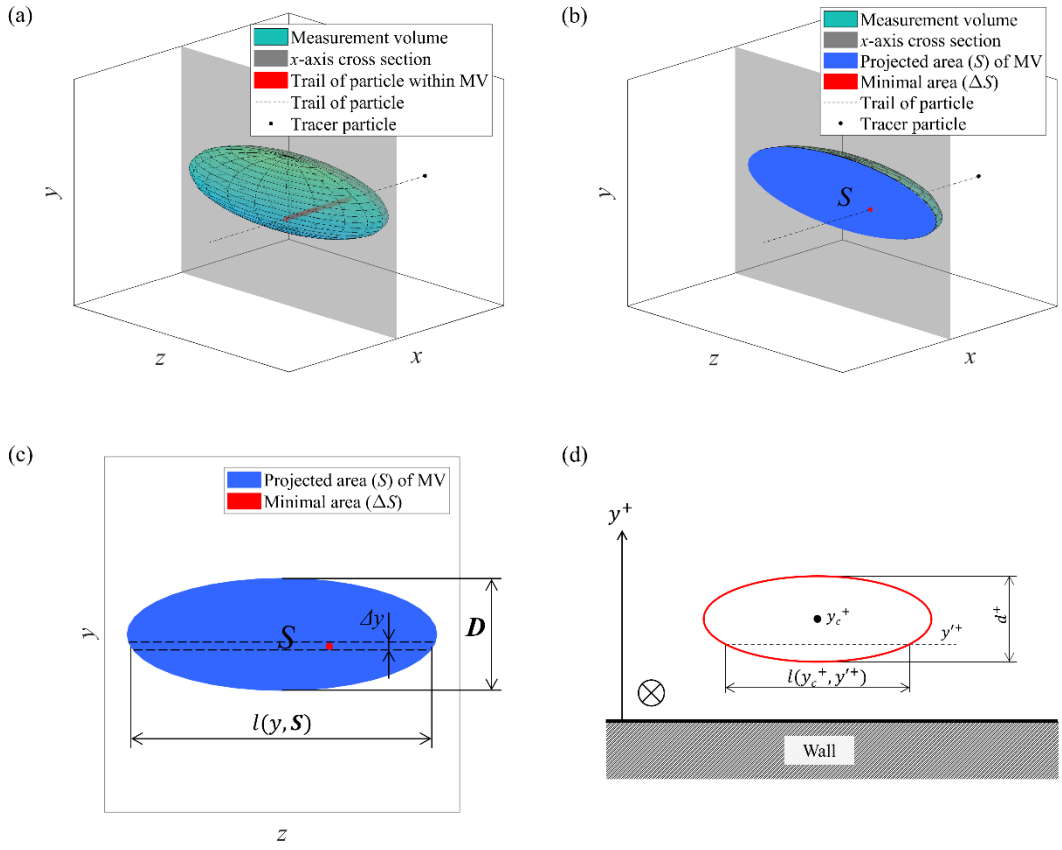

Fig. 2. Schematic images of the LDV measurement volume. (a) Schematic image in three-dimensional. (b) Schematic image sliced at cross-section. (c) Schematic image in two-dimensional. (d) Schematic illustration of the coordinate of the measurement volume.

3.3. Prediction of the true PDF

Since the true PDFs, P_{T}, are required to represent the measured PDF, P_{M}, at an arbitrary location in Eq. (6), the true PDFs should be appropriately predicted to solve Eq. (6). The true PDFs were expressed as Eq. (7), wherein the wall-normal distance was y^{+}, mean velocity was U^{+}, and root mean square (RMS) of the fluctuating velocity was u^{+}_{rms}. The P_{T} in Eq. (6) was replaced by the reference PDF, P_{ref}, in Eq. (7), as follows:

$$P_{\mathrm{T}}(u^{+};y^{+}) = P_{\mathrm{ref}}((u^{+}-U^{+})/u^{+}_{\mathrm{rms}};y^{+})/u^{+}_{\mathrm{rms}}, \tag{7}$$

where P_{ref} was normalized by the standard deviation because the integration of Eq. (7) should yield 1.

From Eq. (7), predicting the true PDF profile is the same as predicting the reference PDF profiles. In the present study, we used the normalized PDFs. According to the evidence of DNS described in Appendix A, we confirmed that the normalized PDFs depend on the distance from the wall but are less dependent of

Reynolds number. Therefore, the reference PDFs were obtained in low Reynolds number flow by LDV with sufficient spatial resolution. There may be other methods to obtain the reference PDFs. Once the reference PDFs were determined, they were applied to the present correction method.

3.4. Formulation for correction

Although the LDV measurement volume effect was expressed by Eq. (6), the theoretical solution of P_T from P_M was difficult because the inverse problem was sensitive to the experimental noise. Therefore, we proposed an alternative procedure based on the discrete expression of Eq. (6) and discuss the effect of the measurement volume on the velocity statistics.

Converting the integral expression of Eq. (6) to a discrete expression, we obtained Eqs. (8) and (9). Equation (8) indicates that the measured PDF was constructed via the summation of the product of the true PDF and tracer particle penetration ratio within the measurement volume at the discretized measurement locations. The finite size effect was equal to the penetration ratio. The penetration ratio is defined by Eq. (9), which indicated the ratio of the cross-sectional partial area at each discretized measurement location to the entire cross-sectional area of the measurement volume.

$$P_M(u^+; y_i^+) = \sum_{j=1}^{n} P_T(u^+; y_j^+) \times F(y_i^+, y_j^+) \tag{8}$$

$$F(y_i^+, y_j^+) = \Delta S(y_i^+, y_j^+) \Big/ \sum_{j=1}^{n} \Delta S(y_i^+, y_j^+) \tag{9}$$

Figure 3 shows a schematic diagram of the above consideration of measurement volume effect described by Eqs. (8) and (9). The measurement volume centered at y_i^+ includes four measurement subsets along with the measurement path. Here, $P_T(u^+, y_j^+)$indicates the true PDF of fluctuating velocity u^+ at the wall-normal location y_j^+. The subscripts *i* and *j* indicate the location of a measurement path. $\Delta S(y_i^+, y_j^+)$ is the streamwise cross-sectional partial area range $(y_j^+ + y_{j-1}^+)/2 \le y^+ < (y_{j+1}^+ + y_j^+)/2$ where the focal point locates at y_i^+, $F(y_i^+, y_j^+)$ is the dominant ratio of $\Delta S(y_i^+, y_j^+)$ to the streamwise entire cross-sectional area of the measurement volume where the focal point locates at y_i^+, and *d* is the wall-normal length of the entire measurement volume. The reason the measurement volume size d^+ was not included in the left-hand side of Eq. (8) was that the measurement volume size already accounted for the calculation of the streamwise cross-sectional partial area. From Eq. (8), the PDF of the velocity measured by the LDV was expressed as the summation of the true PDFs with the penetration ratio under the practical experimental condition.

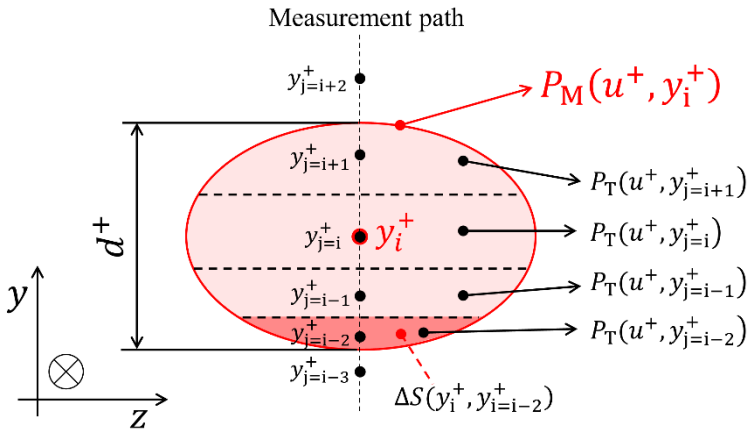

Fig. 3. Conceptual image of measurement volume at PDF calculation in Eq. (8)

By applying the Eqs. (8) and (9) to all measurement locations, the relation among P_T, P_M, and the penetration ratio F was derived as follows:

$$\begin{pmatrix} F_{1,1} & \cdots & F_{1,n} \\ \vdots & \ddots & \vdots \\ F_{n,1} & \cdots & F_{n,n} \end{pmatrix} \begin{pmatrix} P_T(u^+; y_1^+) \\ \vdots \\ P_T(u^+; y_n^+) \end{pmatrix} = \begin{pmatrix} P_M(u^+; y_1^+) \\ \vdots \\ P_M(u^+; y_n^+) \end{pmatrix}, \tag{10}$$

where subscripts i and j in penetration ratio $F_{i,j}$ correspond to the wall-normal distances of y_i and y_j, respectively. $F_{i,j}$ can be calculated from Eq. (9). Although Eq. (10) could be solved analytically as an inverse problem, the experimental uncertainties would affect the result, which would yield a quite different PDF profile from the expected one. Thus, we solved Eq. (10) numerically. The details are in the next subsection.

3.5. Correction procedure

In this subsection, we discuss the correction of the TI profile from the measured TI profile. Solving Eq. (10) numerically, we predicted the TI profile wherein the measurement volume effect was removed and called it the corrected TI profile.

3.5.1. Preprocessing for measured PDF

To obtain the PDF $P_M(u_i)$ in Eq. (8), we should measure the probability $[u_i - \Delta u/2 \leq \eta < u_i + \Delta u/2]$ and divide it by Δu, where η is a random variable in time (or in space). Because of the uncertainty in determining a proper bin size Δu, several Δu values were tested to access whether the obtained PDF profile changed. We selected the smallest bin size that would not distort the PDF profile. The bin size was set to $0.3\,\sigma$ in this analysis, where σ was a standard deviation. The definition range was set to $-9.6\,\sigma < u < 9.6\,\sigma$. Here, the selection of the definition range is independent of the correction results, as long as it

includes the entire measurement velocity range. When the velocity fluctuation u was discretized by the bin size, it was expressed as $u_\mathrm{i} = -9.6\,\sigma + (i - 1/2)\Delta u$ with $i = 1,2,3,\cdots,63,64$. In addition, the measured PDF $P_\mathrm{M}(u_\mathrm{i})$ was expressed as follows:

$$P_\mathrm{M}(u_\mathrm{i}) = \frac{\text{probability}\,[u_\mathrm{i} - \Delta u/2 \le \eta < u_\mathrm{i} + \Delta u/2]}{\Delta u} \times g_\mathrm{i} / \sum_{i=1}^{n} g_\mathrm{i}\,, \qquad (11)$$

$$g_\mathrm{i} = 1/|u_\mathrm{i}|$$

where g_i is the weight factor based on the frequency of the particles passing the measurement volume, namely, the inverse velocity. Nakao *et al.* [21] reported that the time-averaged statistics of velocities measured by LDV can be corrected by an inverse of each particle velocity as a penetration frequency. Since the term including g_i means the correction term for the particle penetration frequency, the probability density of particle velocity can be calculated by a simple multiplication as Eq. (11). This velocity correction method only considered the tracer particles penetration ratio based on the frequency of the particle passing the measurement volume, namely, the inverse velocity. Usually, the passing time through the measurement volume, called the transit time, is recommended for the weight factor [22]. However, since the streamwise velocity component was dominant compared with others for the present flow field, the inverse velocity given in Eq. (11) was available.

3.5.2. Reference PDF profiles

As discussed in Section 3.3, in this study, the reference PDF profiles of fluctuating velocity in the streamwise direction were calculated by the high spatial resolution experimental data at $\mathrm{Re}_\tau < 4000$, which had been obtained in our previous study [3]. The reference PDFs were obtained at 12 wall-normal locations y^+ = 2.5, 5.5, 8.5, 12, 17, 25, 37.5, 57.5, 85, 120, 170, and 250.

Figure 4 shows P_ref at y^+ = 2.5, 8.5, 17, 37.5, 85, and 170. In the different Reynolds number experiments, the measurement points were not the same as those in Fig. 4. Then, the PDF at an arbitrary wall-normal location could be calculated by linear interpolation using two nearby reference PDFs. For example, the reference PDF at y^+ =10 was calculated using the reference PDFs at y^+ = 8.5 and 12. The validity of the use of reference PDF profiles that are independent of Reynolds number in the near-wall region was briefly discussed in Appendix A using DNS data [23,24].

3.5.3. Calculation of the measurement volume size, location, and inclination

In the process of evaluating the measurement volume effects, the measurement volume size, focal point location, and inclination angle of the long axis of measurement volume to the wall need to be precisely calculated. For the calculation, we assumed that the deformation of the laser beam was negligible, the measurement volume located at the focal point as the origin even if the focal point was close to the wall,

and the measurement volume size was equal to the theoretical volume size. The wall-normal length of the measurement volume d was obtained from the accurate calculation of the laser refraction at the surface between a glass pipe wall and a working fluid. Figure 5 shows a typical measurement volume setting under the experiment condition. The wall-normal length of the measurement volume d is used later in the Durst correction method.

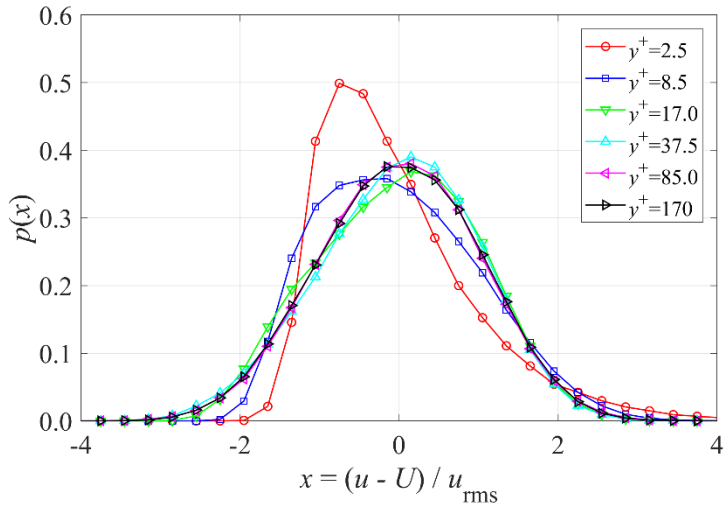

Fig. 4. PDF profiles near-wall region measured at $Re_\tau < 4000$. The red, blue, green, cyan, magenta, and black lines indicate reference PDFs at $y^+ = 2.5$, 8.5, 17, 37.5, 85, and 170, respectively.

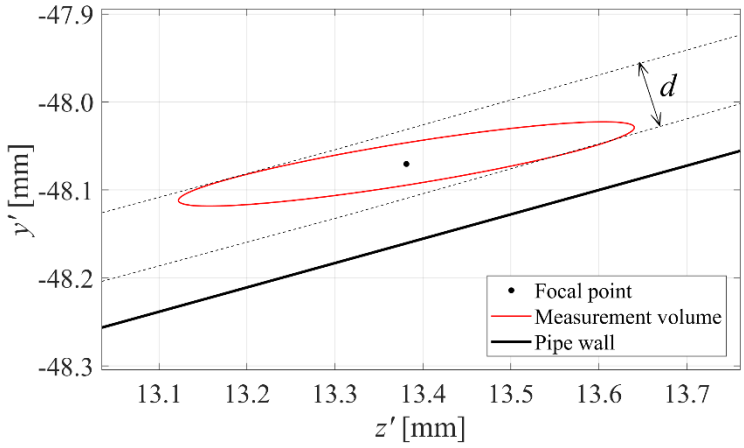

Fig. 5. Schematic image of measurement volume location. The dot indicates a focal point, the red ellipse indicates a measurement volume, the bold black line indicates the pipe wall, and the dashed lines indicate a maximum and a minimum distance from the wall.

3.5.4. Calculation of penetration ratio of tracer particles

Calculation of the penetration ratio of tracer particles passing through the measurement volume was a crucial process in the entire correction procedure because the matrix of the penetration ratio was used in Eq. (10). Since the penetration ratio was calculated from Eq. (9), the streamwise cross-sectional area of the measurement volume was necessary. The location and inclination angle of the measurement volume were calculated in Section 3.5.3, and using this information, the penetration ratio of each measurement location within the measurement volume at the target wall-normal location could be calculated. Figure 6 shows a measurement volume centered at the point indicated by a black dot. The measurement area is divided into subsets between two adjacent dashed lines. Comparing with Fig. 3, the focal point is y_i, and the red area in Fig. 6 indicates $\Delta S(y_i, y_{i-2})$; then, the penetration ratio $F_{i,i-2}$ is calculated as $\Delta S(y_i, y_{i-2})/S$.

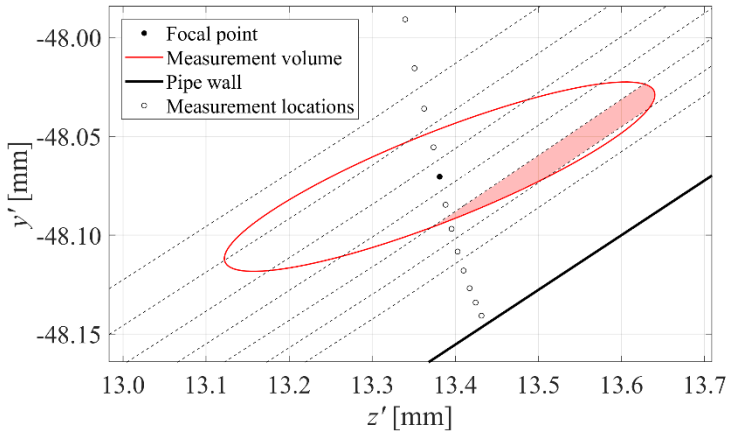

Fig. 6. Example of measurement volume, pipe wall, and each measurement location for calculation of penetration ratio of tracer particles. The red ellipse and bold black line indicate the boundary of the theoretical measurement volume and wall, respectively. The black circles indicate measurement locations corresponding to the focal points of the LDV in the experiment. The dashed lines indicate an intermediate wall-normal position between two adjacent measurement locations.

3.5.5. Correction procedure

The true PDF, P_T, defined in Eq. (7), the measured PDF, P_M, defined in Eq. (11), and the penetration ratio, $F_{i,j}$, as mentioned in Section 3.5.4, were inserted in Eq. (10). This relation expressed how the measured PDFs related to the true PDFs. The true PDFs can be replaced by the reference PDFs, as shown in Eq. (7), but the u^+_{rms} is not previously known. Therefore, in this study, u^+_{rms} in Eq. (7) was determined as follows. For simplicity, u^+_{rms} at y_i is written as $rms(y_i)$ hereinafter.

First, the initial RMS value $rms^0_{cor}(y_i) = rms_{meas}(y_i)$ was inserted into Eq. (7), and the true PDF $P^0_T(y_i)$ was obtained. Adopting $P^0_T(y_i)$ on the left-hand side of Eq. (10), the PDF $P^0_{M,cal}(y_i)$ was derived.

By using $P^0_{\mathrm{M,cal}}(y_\mathrm{i})$, $rms^0_{\mathrm{cal}}(y_i)$ was calculated; it was different from the measured value $rms_{\mathrm{meas}}(y_i)$. Then, the loss function for the optimization process is defined as follows:

$$L^{\mathrm{n}} = \sum_{i=1}^{N} [rms^{\mathrm{n}}_{\mathrm{cal}}(y_i) - rms_{\mathrm{meas}}(y_i)]^2, \tag{12}$$

where N is the total number of measurement locations in the experiment and the superscript n means an iteration count. L^{n} means the loss function at the iteration count of n. The expression of L^{n} is used when focusing on a value of the loss function at a particular iteration count, whereas the expression of L is used when focusing on the general value of the loss function. The input $rms^{\mathrm{n}}_{\mathrm{cor}}(y_i)$ $(n = 1,2,3,\cdots)$ for Eq. (7) is calculated using the following:

$$rms^{\mathrm{n}}_{\mathrm{cor}}(y_\mathrm{i}) = rms^{\mathrm{n-1}}_{\mathrm{cor}}(y_\mathrm{i}) - \frac{\partial L^{\mathrm{n\text{-}1}}}{\partial\, rms^{\mathrm{n-1}}_{\mathrm{cor}}(y_\mathrm{i})} \times \alpha, \tag{13}$$

where $rms^{\mathrm{n}}_{\mathrm{cor}}$ means the corrected TI value by the present optimization process, α is a parameter to determine the weight for optimization, and it is 0.2 in the present analysis. When the loss function L^{n} is smaller than 0.1, $rms^{\mathrm{n}}_{\mathrm{cor}}$ is expressed as $u^{+}_{\mathrm{rms,cor}}$ and the PDFs on the right-hand side of Eq. (10) are $P_{\mathrm{M,cal}}$. Notably, $P_{\mathrm{M,cal}}$ is not the same as P_{M}, which represent the PDFs measured in the experiment. The threshold value 0.1 and parameter α were determined by the n dependence of the loss function L and the value of TI profile, as described in Appendix B.

4. Results and discussions

4.1. PDF profile prediction by Eq. (8)

In this subsection, the validity of the proposed correction method is confirmed. Figure 7 shows the PDF profiles at low Reynolds number contrasted between the measured result and the predicted one by Eq. (8). These partial PDF profiles correspond to each component on the right-hand side of Eq. (8). The summation of the color lines equals the red bold solid line. From the figure, the measured and predicted profiles overlapped. Thus, it was confirmed that the PDF profile of fluctuating velocity measured by LDV could be expressed by summing the reference PDF profiles with the weighing factors. From this result, the validity of Eq. (8) was confirmed.

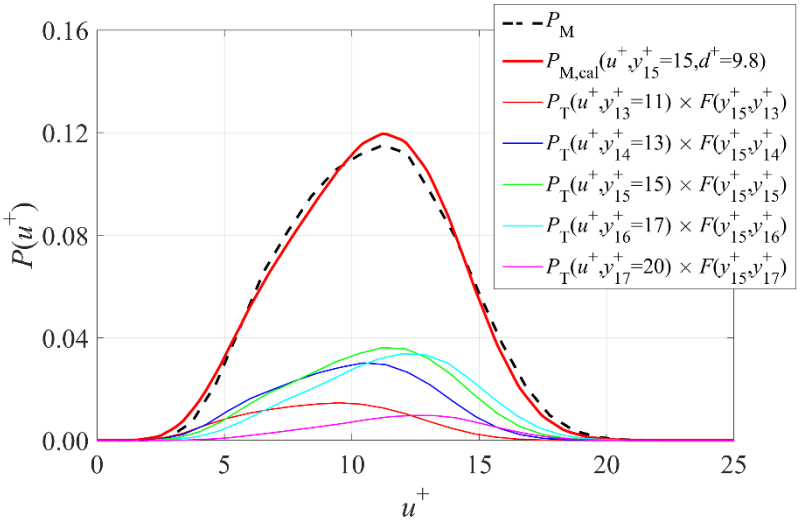

Fig. 7. Comparison of the measured PDF and PDF predicted by Eq. (8) at $Re_\tau = 3200$ in case 3. The black dashed and red bold solid lines indicate the measured PDF profile P_M and predicted PDF profile $P_{M,cal}$ using Eq. (8) at $y^+ = 15$, respectively. The other color lines indicate partial PDF profiles at each wall-normal location at $y^+ = 11$, 13, 15, 17, and 20, respectively.

4.2. Correction results of TI profile

4.2.1. Comparison with different spatial resolution conditions

In this subsection, the TI profiles at $Re_\tau = 3200$ corrected by the proposed correction method are discussed. Figures 8 (a–c) show the TI profiles measured by LDV under Cases 1–3, respectively. In each figure, it is observed that the corrected TI values are equal to or lower than the measured ones. It can be seen that the lower the spatial resolution, the larger the measured TI values, especially near the wall. Since the TI values measured by LDV overestimate the true ones, the proposed correction method works well to diminish the measurement volume effect on the TI values measured by LDV. Figure 8 (d) shows a comparison between the corrected TI profiles under different spatial resolution conditions. Although the corrected TI profiles showed slight differences among each other, the corrected TI profiles based on the measured TI profiles under different spatial resolution conditions at the same Reynolds number overlapped and agreed with pipe DNS data by Ahn *et al*. [25]. We observed the difference depending on the spatial resolution in the near-wall region ($y^+ < 10$). It was due to the uncertainties of the LDV measurement volume size and measurement location. From these results, the proposed correction method works well to correct the TI profile measured by LDV with the finite measurement volume and gives a reasonable correction result under the three cases.

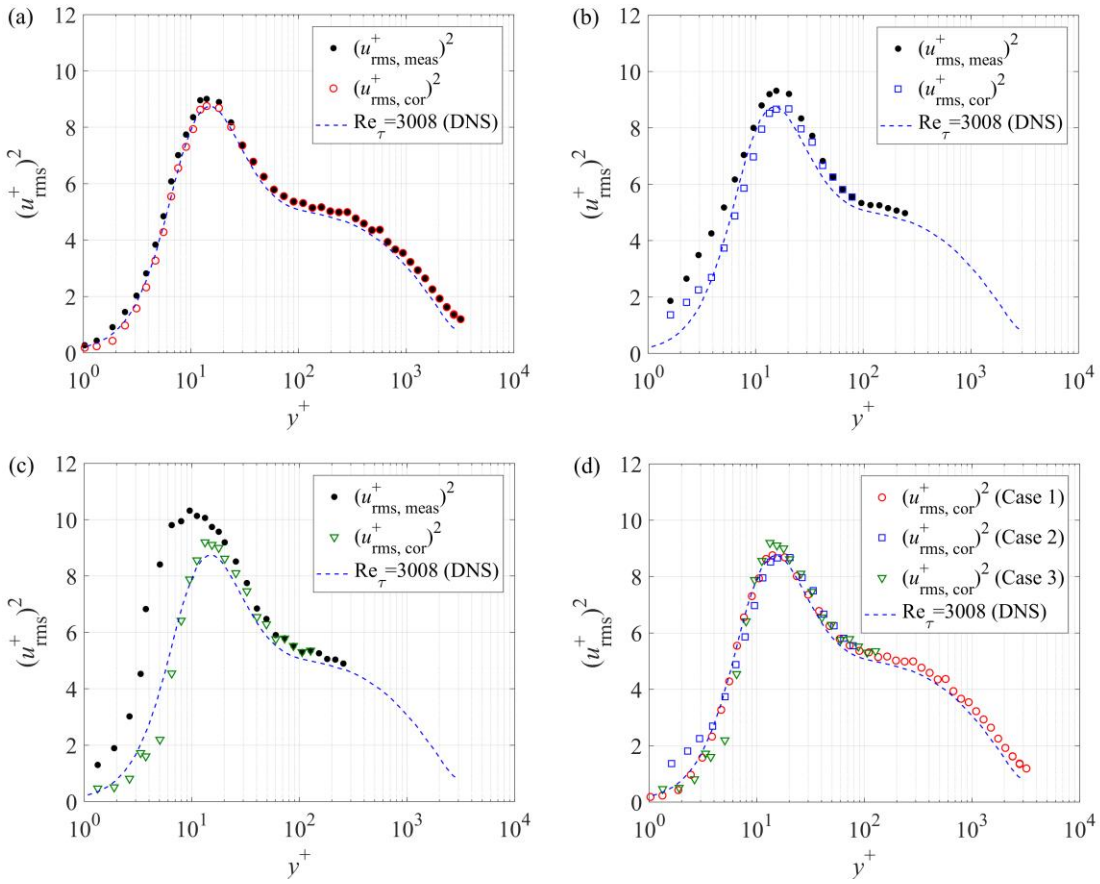

Fig. 8. Comparison of the corrected and measured TI profiles at Re_τ = 3200 with different spatial resolution. (a) Case 1; (b) Case 2; (c) Case 3; (d) Comparison of corrected profiles. The black solid circles indicate the measured TI profile $u^+_{rms,meas}$; the red open circles, blue open squares, and green open triangles indicate the corrected TI profile $u^+_{rms,cor}$ in Cases 1–3, respectively. The dashed line indicates pipe DNS data by Ahn, *et al*. [25] at Re_τ = 3008.

4.2.2. Comparison with Durst correction method

In this subsection, the proposed correction method is compared with that of Durst *et al.* [8]. The latter one has only been confirmed at low Reynolds numbers; therefore, its applicability to high Reynolds numbers is worth discussing. Before the comparison of results, the Durst method is briefly explained.

The LDV measurement volume effect was investigated by Durst *et al.* [8]. Their concept for the LDV measurement volume effect is based on the laser intensity profile within the LDV measurement volume, which means that an obtained velocity measured by LDV with a finite measurement volume is considered a volumetric average value within the measurement volume. Therefore, their correction process for the measurement volume effect is based on the volumetric integration within the measurement volume. The correction equations for the mean and RMS values are, respectively, described by Eqs. (14) and (15).

$$\overline{U}_{\mathrm{meas}} = \overline{U}_{\mathrm{true}} + \frac{d^2}{32}\left(\frac{d^2\overline{U}_{\mathrm{true}}}{dy^2}\right), \tag{14}$$

$$\overline{u^2}_{\mathrm{meas}} = \overline{u^2}_{\mathrm{true}} + \frac{d^2}{32}\left[2\left(\frac{d\overline{U}_{\mathrm{true}}}{dy}\right)^2 + \left(\frac{d^2\overline{u^2}_{\mathrm{true}}}{dy^2}\right)\right], \tag{15}$$

where the subscripts “meas” and “true” indicate the measured data with the measurement volume of d and the true data with an infinitely small measurement volume, respectively. This correction method had been used by Fischer *et al.* [9]; they reported that this correction method could provide an appropriate result.

In the correction procedure of the Durst method, we used the measured data for the second term on the right-hand side of Eqs. (14) and (15). In addition, the derivatives were calculated from the second-order accuracy.

Figure 9 shows a comparison of the original TI profile measured by LDV, the corrected TI profiles by the Durst and proposed methods, pipe experimental data by Hultmark *et al*. [6] and Willert *et al*. [10], pipe DNS data by Ahn *et al*. [25] and Pirozzoli *et al*. [26], and channel DNS data by Yamamoto and Tsuji [23]. Figures 9 (a–c) show the results under different spatial resolution conditions listed in Table 1. From these figures, although both corrected profiles are slightly different, the trends of their near-wall profiles are almost the same and in agreement with the previous study data. Although the two correction methods are based on different fundamental concepts, they provide almost the same correction results. Therefore, the fundamental concept of each correction method is appropriate.

4.2.3. Applicability to relatively high Reynolds numbers

In this subsection, the applicability of both correction methods to relatively high Reynolds numbers up to $\mathrm{Re}_\tau = 10000$ is discussed. Figures 9 (d–f) show the measured TI profile and two corrected TI profiles under 3 different Reynolds number conditions with high spatial resolution settings. From these figures, comparing the measured TI profile with the previous study data, we observed the spatial resolution effect. That is, the TI values increased in the near-wall region in the relatively high Reynolds number region. Although the corrected TI profiles are slightly different, the trends of their profiles are similar and in agreement with those of the previous study. At approximately $y^+ = 15$, where the TI profile has an inner peak, both the proposed and Durst methods give consistent results, even at high Reynolds numbers up to $\mathrm{Re}_\tau = 10000$, and inclined measurement volume condition in the comparison with the previous study. Furthermore, the corrected TI profiles were in good agreement with the previous experimental and numerical data even in the near-wall region ($y^+ < 10$). For the applicability of the correction methods to the increased Reynolds numbers, both correction methods are likely to correct the TI profiles, as long as the LDV measurement volume size and location are properly determined.

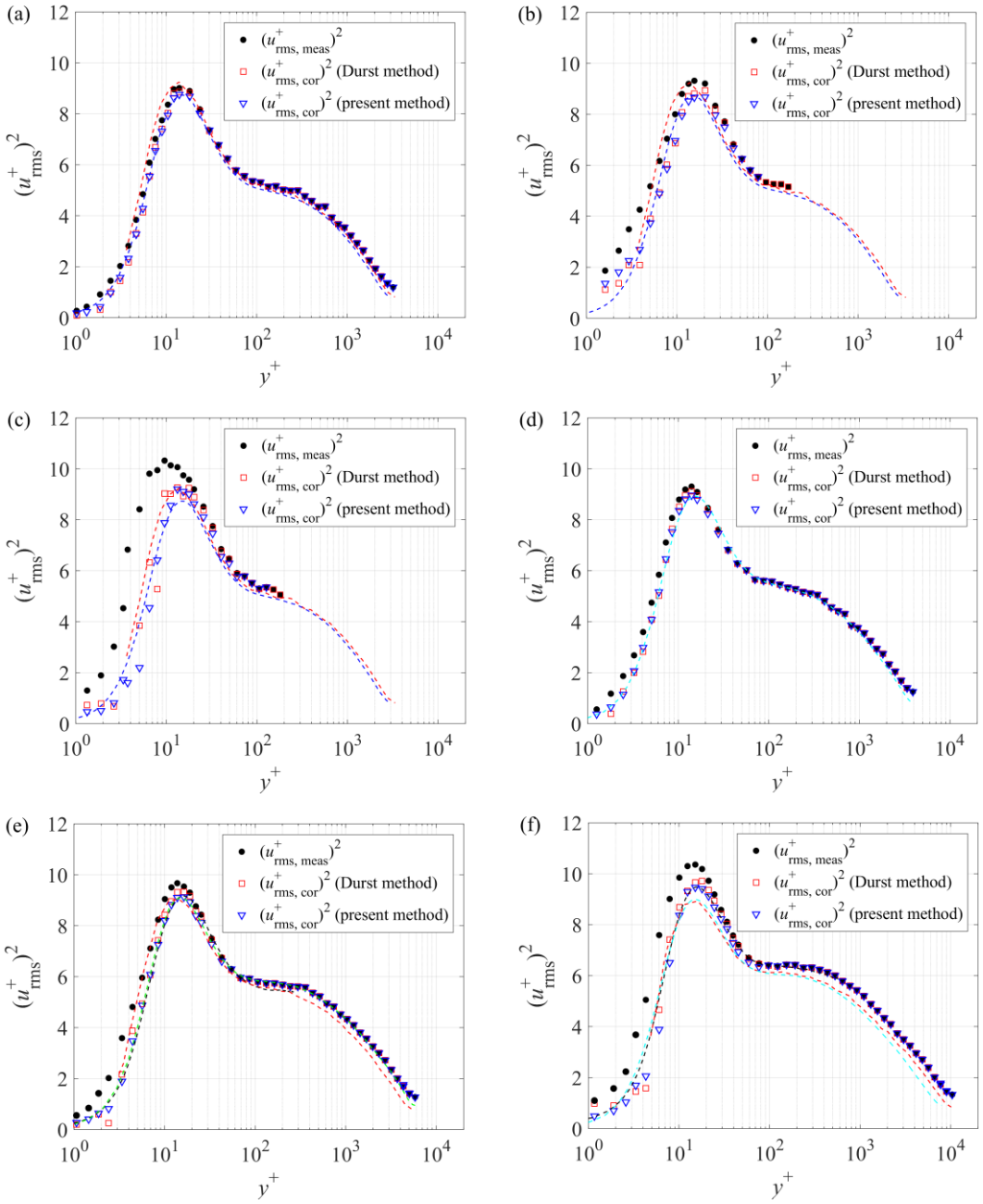

Fig. 9. Comparison of TI profiles corrected by Durst and proposed methods. (a) $Re_\tau = 3200$ in Case 1; (b) $Re_\tau = 3200$ in Case 2; (c) $Re_\tau = 3200$ in Case 3; (d) $Re_\tau = 3900$ in Case 1; (e) $Re_\tau = 5800$ in Case 1; (f) $Re_\tau = 10400$ in Case 1. The black solid circles indicate the measured TI profile, the red squares indicate the corrected TI profile by the Durst method, and the blue triangles indicate the corrected TI profile by the proposed method. The black and red dashed lines indicate pipe experimental data by Willert, *et al.*[10] at $Re_\tau = 5358$ and 11708 and Hultmark, *et al.*[6] at $Re_\tau = 3334$, 5411, and 10480. The blue, green, and light blue dashed lines indicate DNS data by Ahn *et al.* [25] at $Re_\tau = 3008$ (pipe), Pirozzoli *et al.* [26] at $Re_\tau = 6000$ (pipe), and Yamamoto and Tsuji [23] at $Re_\tau = 4000$ and 8000 (channel).

4.3. Discussions

By comparing the corrected TI profiles, as shown in Fig. 9, we confirmed that the result from the Durst and present methods are comparable. In this subsection, we summarize the difference between the present and the Durst method. Further, their advantages and disadvantages are mentioned in terms of correction procedure and further applicability.

The difference between the present and the Durst methods concerns the velocity detection frequency in the LDV measurement. The Durst method considered that the velocity detection frequency increases in the region where the laser intensity is relatively strong, and the time-averaged statistics can be calculated by the weighting average of the laser intensity in a general velocity field. In contrast, the present method considered a tracer particle penetration frequency using the measurement volume without laser intensity. Based on the geometric consideration, the time-averaged statistics can be calculated by the streamwise cross-sectional average of the time-averaged statistics in the infinitesimal measurement volume.

For the correction procedure, since the Durst method can correct the profile using measured profile explicitly by Eqs. (14) and (15), it is easy to apply the Durst method. In contrast, the present correction procedure is more complex than the Durst method. Therefore, the complexity of the correction procedure is a disadvantage of the present method.

For further application, the present method can be easily combined with other corrections, such as a bias of velocity measurement. A fringe distortion is an example of the bias of velocity measurement. In general, the fringe spacing constructed in the measurement volume should be constant within the measurement volume. However, under some conditions, the fringe spacing is distorted within the measurement volume. The present method can simultaneously correct the effects of fringe distortion and spatial resolution by incorporating the fringe distortion effects to the “true” PDF calculation step in the present correction procedure. This is an advantage of the present method. We are now summarizing another paper on the fringe distortion effect.

As described above, there are several advantages and disadvantages to each correction. However, there is no significant difference in the corrected turbulence intensity profiles between the Durst and present methods.

5. Conclusions

A new correction method for LDV measurement volume effects on time-averaged velocity statistics was proposed. The proposed correction method is based on the geometric consideration of a measurement volume and the PDF of velocity fluctuation. The obtained results are summarized as follows.

- The measurement volume effect on the PDF of the streamwise velocity is expressed by Eq. (4) from the consideration of the measurement volume geometry and the probability of particle penetration for the steady flow fields.

- The proposed correction method is performed for turbulent pipe flow data. In the correction procedure, the PDF profiles measured at low Reynolds numbers are used as the reference PDF profiles. The correction is conducted using the measured TI profile as an initial profile, and then the corrected TI profile is obtained by optimization.
- The predicted PDF profile based on Eq. (8) agrees well with the measured PDF profile, which is affected by the measurement volume. From this result, the validity of the principle of the proposed correction method using PDF is confirmed. The corrected TI profiles based on the measured TI profile under different spatial resolution conditions at $Re_\tau = 3200$ collapsed with each other and agreed with DNS data; therefore, we confirmed the validity of applying the proposed correction method.

We compared the corrected TI profiles by the proposed correction method with that of Durst *et al.* [8] and found that the results are almost identical, although they have different fundamental concepts. This conclusion means that both correction methods guarantee the validity of data correction. We also confirmed the validity of the proposed correction method for high Reynolds numbers of up to $Re_\tau = 10000$ and for the inclined measurement volume of LDV by comparison with the previous experimental and numerical studies.

Acknowledgment

I would like to thank Professor Yoshinobu Yamamoto of the University of Yamanashi for providing the channel DNS data to discuss Re-dependence of the streamwise fluctuating velocity PDF. This work is partially supported by "Nagoya University High Performance Computing Research Project for Joint Computational Science" in Japan. This work was supported by JSPS KAKENHI [grant numbers JP15H03923, JP15H03917].

Appendix A: Confirmation of Reynolds number dependence (Re-dependence) of near-wall PDFs normalized by its mean and standard deviation using channel DNS data

In the proposed correction method, we used normalized PDFs measured at low Reynolds numbers as reference PDFs in the near-wall region at various Reynolds numbers. In this appendix, to confirm the validity of the prediction for reference PDF, a discussion of Re-dependence of the near-wall PDFs using channel DNS data of up to $Re_\tau = 8000$ by Yamamoto [24]. To evaluate the differences of PDFs among Reynolds numbers, Gram–Charlier series for Gaussian profile was used as reported by Tsuji *et al.* [27]. The series are indicated as Eqs. (A.1) and (A.2).

$$P_{\mathrm{y}}(u) = c_0\phi(u) + \frac{c_1}{1}\phi'(u) + \frac{c_2}{2}\phi''(u) + \cdots + \frac{c_2}{n!}\phi^{(\mathrm{n})}(u), \tag{A.1}$$

$$\phi^{(\mathrm{n})}(u) = (-1)^{\mathrm{n}} H_{\mathrm{n}}(u)\phi(u), \tag{A.2}$$

where $H_n(x)$ is the Hermite function, and $\phi(x)$ is the Gaussian PDF. Figures A.1 (a) and (b) show the comparison of PDFs at different Reynolds numbers at the wall-normal distance of y^+=5 and 15, respectively. From these figures, although the Re-dependence of PDF profiles slightly differs, their general tendencies are identical. Figures A.2 (a) and (b) show the Gram–Charlier series coefficients. From these figures, although the differences of coefficients are found to be relatively larger for coefficients more than the fifth order, it is considered that the Re-dependence of coefficients less than the fourth order is almost negligible. From the above comparisons, the Re-dependence of PDF profiles, especially in the near-wall region, is almost negligible for applying the proposed correction method at target Reynolds number range.

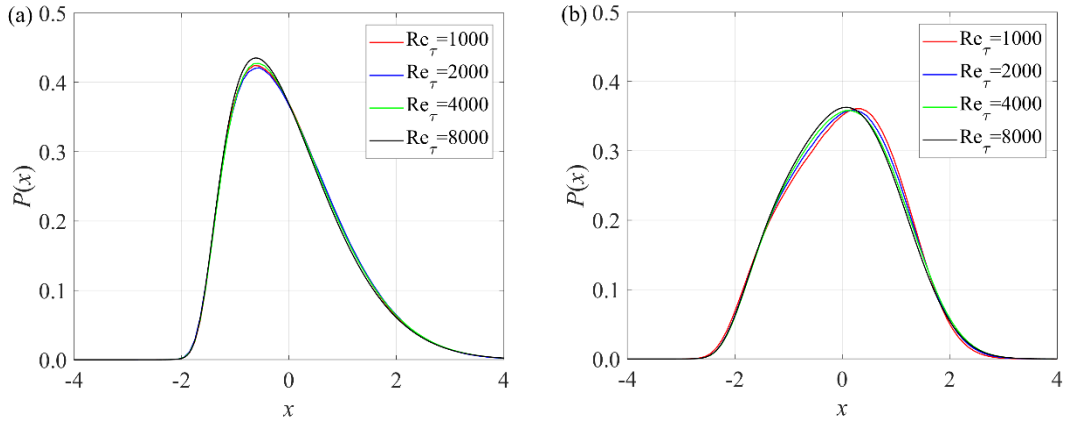

Fig. A.1. Comparison of PDF profiles using DNS data. (a) PDFs at y^+=5; (b) PDFs at y^+=15. The red, blue, green, and black lines indicate PDF profiles at Re_τ = 1000, 2000, 4000, and 8000, respectively.

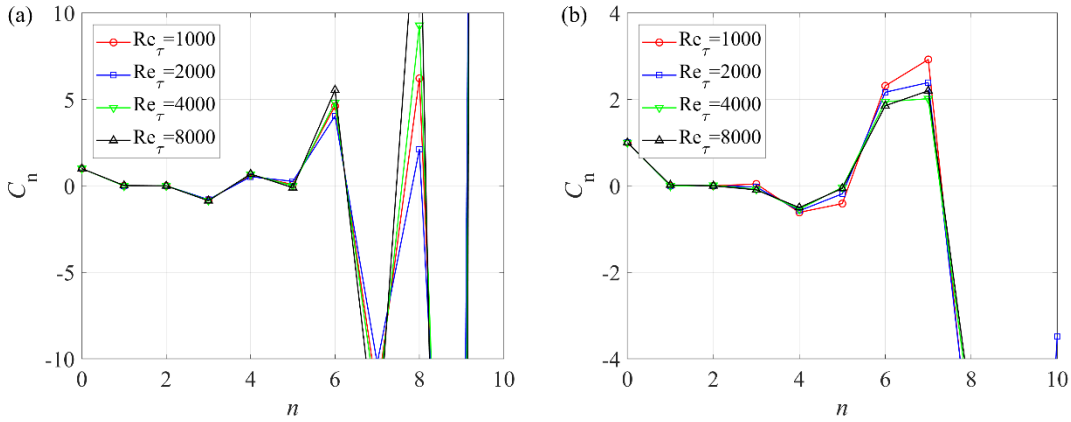

Fig. A.2. Comparison of Gram–Charlier series coefficient. (a) y^+=5; (b) y^+=15. The red, blue, green, and black lines indicate Gram–Charlier series coefficients at Re_τ = 1000, 2000, 4000, and 8000, respectively.

Appendix B: Determination of optimization parameters

In the proposed correction method, the optimization process using gradient descent was used. This appendix shows how the optimization parameter α in Eq. (13) and a threshold value of the loss function expressed by Eq. (12) are determined.

Figure B.1 (a) shows the iteration count n dependence of the loss function L for various α values. Each loss function value decreases as the iteration count increases, which means that the calculated TI profile approaches the measured one. For the larger α value, the larger decrease rate of L. Generally, a large decrease rate is preferred for optimization, but the rate of α = 0.4 is overlarge. Therefore, we concluded that α = 0.2 is a rational decrease rate for the present optimization process.

Figure B.1 (b) shows a comparison of the measured TI profile with the calculated TI profiles in the optimization process at n = 0, 3, 6, 9, and 12 in Case 3 at Re_τ = 3200 [Fig. 8 (c)]. The black solid circles indicate the measured TI profile, each color line indicates the calculated TI profiles based on Eq. (10) at n = 0, 3, 6, 9, and 12, and the value of the loss function at each n is given in the explanatory notes. From Fig. B.1 (b), by increasing the iteration count or decreasing the loss function value, the calculated TI profile approaches the measured profile. At n =12 and L^{12} = 0.09, the calculated TI profile agrees with the measured TI profile. Figure B.1 (c) shows the L dependence of the calculated TI profile. Although a smaller value of L means that the calculated TI profile matches better with the measured one, the degree of agreement is almost identical at $L \leq 0.1$ from Fig. B.1 (c). Figure B.1 (d) shows the L dependence of the corrected TI profile. From this figure, the corrected TI profiles at $L \leq 0.05$ had an irregular profile, which would come from overoptimization. Therefore, we concluded that 0.1 is a rational threshold value of L to finish the optimization process and determine the corrected TI profile.

From the above discussions, the parameter α = 0.2 and the threshold of L = 0.1 are suitable values for the optimization process described in Section 3.5.5. From Figs. B.1 (b–d), the present optimization process gives a rational corrected TI profile for the measurement volume effect.

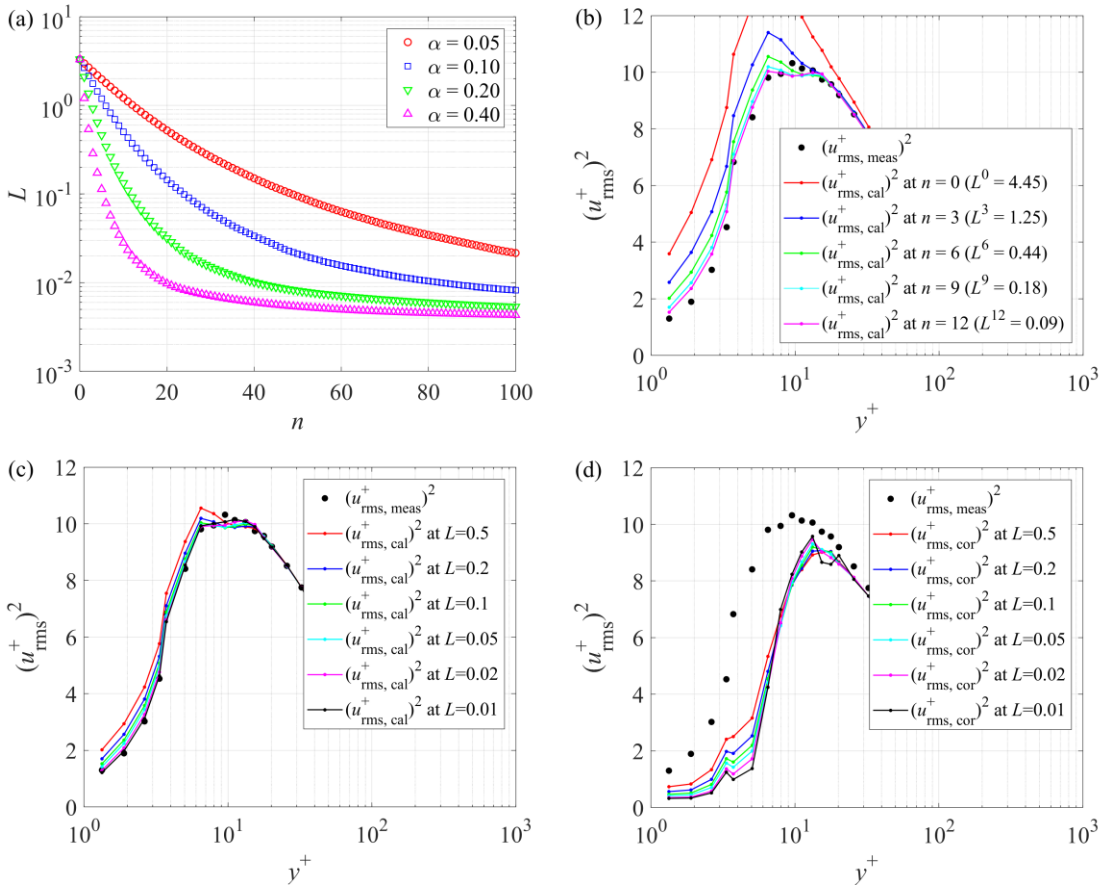

Fig. B.1. Parameter dependence of optimization process in Case 3 at $Re_\tau = 3200$. (a) Iteration count dependence of the loss function for various α; (b) Calculated TI profiles for various n with $\alpha = 0.2$; (c) Calculated TI profiles for various L with $\alpha = 0.2$; (d) Corrected TI profiles for various L with $\alpha = 0.2$.

References

[1] M. V. Zagarola and A. J. Smits, Mean-flow scaling of turbulent pipe flow, J. Fluid Mech. **373**, 33 (1998).

[2] A. Talamelli, F. Persiani, J. H. M. Fransson, P. H. Alfredsson, A. V. Johansson, H. M. Nagib, J. D. Rüedi, K. R. Sreenivasan, and P. A. Monkewitz, CICLoPE-a response to the need for high Reynolds number experiments, Fluid Dyn. Res. **41**, 021407 (2009).

[3] N. Furuichi, Y. Terao, Y. Wada, and Y. Tsuji, Friction factor and mean velocity profile for pipe flow at high Reynolds numbers, Phys. Fluids **27**, 095108 (2015).

[4] B. J. McKeon, J. Li, W. Jiang, J. F. Morrison, and A. J. Smits, Further observations on the mean velocity distribution in fully developed pipe flow, J. Fluid Mech. **501**, 135 (2004).

[5] J. F. Morrison, B. J. McKeon, W. Jiang, and A. J. Smits, Scaling of the streamwise velocity component in turbulent pipe flow, J. Fluid Mech. **508**, 99 (2004).

[6] M. Hultmark, S. C. C. Bailey, and A. J. Smits, Scaling of near-wall turbulence in pipe flow, J. Fluid Mech. **649**, 103 (2010).

[7] F. König, El-S. Zanoun, E. Öngüner, and C. Egbers, The CoLaPipe-The new Cottbus large pipe test facility at Brandenburg University of Technology Cottbus-Senftenberg, Rev. Sci. Instrum. **85**, 075115 (2014).
[8] F. Durst, J. Jovanovic, and J. Sender, LDA measurement in the near-wall region of a turbulent pipe flow, J. Fluid Mech. **295**, 305 (1995).
[9] M. Fischer, J. Jovanovic, and F. Durst, Reynolds number effects in the near-wall region of turbulent channel flows, Phys. Fluids **13**, 1755 (2001).
[10] C. E. Willert, J. Soria, M. Stanislas, J. Klinner, O. Amili, M. Eisfelder, C. Cuvier, G. Bellani, T. Fiorini, and A. Talamelli, Near-wall statistics of a turbulent pipe flow at shear Reynolds numbers up to 40 000, J. Fluid Mech. **826**, 1 (2017).
[11] D. B. De Graaff and J. K. Eaton, Reynolds-number scaling of the flat plate turbulent boundary layer, J. Fluid Mech. **422**, 319 (2000).
[12] I. Marusic, B. J. McKeon, P. A. Monkewits, H. M. Nagib, A. J. Smits, and K. R. Sreenivasan, Wall-bounded turbulent flows at high Reynolds numbers: Recent advances and key issues, Phys. Fluids **22**, 065103 (2010).
[13] N. Hutchins and I. Marusic, Evidence of very long meandering features in the logarithmic region of turbulent boundary layers, J. Fluid Mech. **579**, 1 (2007).
[14] N. Hutchins, T. B. Nickels, I. Marusic, and M. S. Chong, Hot-wire spatial resolution issues in wall-bounded turbulence, J. Fluid Mech. **635**, 103 (2009).
[15] R. Örlü and P. H. Alfredsson, On spatial resolution issues related to time-averaged quantities using hot-wire anemometry, Exp. Fluids **49**, 101 (2010).
[16] A. J. Smits, J. Monty, M. Hultmark, S. C. C. Bailey, N. Hutchins, and I. Marusic, Spatial resolution correction for wall-bounded turbulence measurements, J. Fluid Mech. **676**, 41 (2011).
[17] A. Segalini, R. Örlü, P. Schlatter, P. H. Alfredsson, J. D. Rüedi, and A. Talamelli, A method to estimate turbulence intensity and transverse Taylor microscale in turbulent flows from spatially averaged hot-wire data, Exp. Fluids **51**, 693 (2011).
[18] N. Furuichi, Y. Terao, Y. Wada, and Y. Tsuji, Further experiments for mean velocity profile of pipe flow at high Reynolds number, Phys. Fluids **30**, 055101 (2018).
[19] N. Furuichi, Y. Terao, and M. Takamoto, Calibration facilities for water flowrate in NMIJ, Proceeding of 7th ISFFM, (Anchorage, USA), (2009).
[20] S. B. Pope, Turbulent Flows, Cambridge University Press, Cambridge, U.K.; New York, U.S.A. (2000).
[21] S. Nakao, Y. Terao, and K. Hirata, New method for eliminating the statistical bias in highly turbulent flow measurements, AIAA Journal **25**, 443 (1987).
[22] R.V. Edwards, Report of the special panel on statistical particle bias problems in laser anemometry, J. Fluids Eng. **109**, 89 (1987).
[23] Y. Yamamoto and Y. Tsuji, Numerical evidence of logarithmic regions in channel flow at $Re_\tau = 8000$, Phys. Rev. Fluids **3**, 012602 (2018).
[24] Y. Yamamoto (private communication).
[25] J. Ahn, J. H. Lee, J. Lee, J. Kang, and H. J. Sung, Direct numerical simulation of a 30R long turbulent pipe flow at $Re_\tau = 3008$, Phys. Fluids **27**, 065110 (2015).
[26] S. Pirozzoli, J. Romero, M. Fatica, R. Verzicco, and P. Orlandi, Reynolds number trends in turbulent pipe flow: a DNS perspective.
[27] Y. Tsuji, B. Lindgren, and A. V. Johansson, Self-similar profile of probability density functions in zero-pressure gradient turbulent boundary layers, Fluid Dyn. Res. **37**, 293 (2005).